Computer Modeling in Engineering & Sciences
DOI:10.32604/cmes.2020.010927
Article

Thermodynamics of Molten Pool Predicted by Computational Fluid Dynamics in Selective Laser Melting of Ti6Al4V: Surface Morphology Evolution and Densification Behavior

Donghua Dai[1,2], Dongdong Gu[1,2,*], Qing Ge[1,2], Chenglong Ma[1,2], Xinyu Shi[1,2] and Han Zhang[1,2]

[1]College of Materials Science and Technology, Nanjing University of Aeronautics and Astronautics, Nanjing, 210016, China
[2]Jiangsu Provincial Engineering Laboratory for Laser Additive Manufacturing of High-Performance Metallic Components, Nanjing University of Aeronautics and Astronautics, Nanjing, 210016, China
*Corresponding Author: Dongdong Gu. Email: dongdonggu@nuaa.edu.cn
Received: 19 April 2020; Accepted: 29 May 2020

Abstract: The three-dimensional physical model of the randomly packed powder material irradiated by the laser beam was established, taking into account the transformation of the material phase, the melt spreading and the interaction of the free surface of the molten pool and the recoiling pressure caused by the material evaporation during the selective laser melting. Influence of the processing parameters on the thermal behavior, the material evaporation, the surface morphology and the densification behavior in the connection region of the molten pool and the substrate was studied. It was shown that the powder material underwent the transformation from the partial melting state to the complete melting state and finally to the overheating state with the applied laser energy density increasing from 167 J/mm^3 to 417 J/mm^3. Therefore, the solidified track ranged from the discontinuous tracks with the rough surface to the continuous tracks with residual porosities, then to the continuous and dense tracks and terminally to the fluctuated tracks with the increase in the laser energy density. Meanwhile, the laser energy effect depth was maintained the positive relationship with the laser energy density. The vortex velocity obtained in the free surface of the molten pool towards to the rear region in the opposite laser scan direction promoted the melt convection to the edge region of the molten pool as the laser energy density was higher than 277 J/mm^3, demonstrating the efficient energy dissipation from the center of the irradiation region to the whole part of the molten pool and the attendant production of the sufficient melt volume. Therefore, the efficient spreading of the molten pool and the metallurgical bonding ability of the melt with the substrate was obtained at the optimized laser energy density of 277 J/mm^3. However, the severe material evaporation would take place as the melt was overheated, resulting in the formation of the residual pores and poor surface quality.

Keywords: Additive manufacturing; melt convection; surface morphology; densification behavior; numerical simulation

1 Introduction

Titanium alloy Ti6Al4V, as the typical two types of the crystal structure: α-phase (the hexagonal closed packed structure) and β-phase (the body-centered cubic structure), has been widely applied in the aeronautical, the military and the biomedical industries due to the outstanding mechanical and physical properties [1,2]. With the increased demand in the complex structures and the high performance, the conventional manufacturing process has encountered large challenges especially in the manufacturing of the internal gradual channels, the ultrathin wall and the gradient lattice structures [3,4]. To realize the reasonable supplement of the manufacturing process, selective laser melting (SLM), as one of the vigorous additive manufacturing processes, has attracted extensive attentions for the production of the metal components [5–7]. The fabrication principles of the SLM of the desired parts are based on the laser selective scanning on the powder material in the track by track and the layer by layer manner dependent on the slicing data and, the metallurgical bonding tracks and layers with the successive tracks and layers are obtained [8]. Repeating this process, the terminal parts without the restrictions of the complex shapes are produced. In spite of the advantages of the free form manufacturing process, the metallurgical defects, such as the residual pores and poor surface morphology, are considerably detrimental to the densification behavior and the performance of the as-fabricated parts, which is mainly caused by the unstable thermocapillary convection and the multi-modes of the heat and mass transform within the molten pool due to the high energy laser beam induced rapid heating and rapid cooling [9,10]. The surface morphology and the relative density of the metallic parts have a key effect of the wear, the fatigue and the performance life of the components [11].

The densification behavior of the SLM process of Ti6Al4V material through the experimental method has been investigated by many researchers. The influence of the processing parameters on the densification, the roughness and the microhardness of the SLM-processed Ti6Al4V components was studied by Song et al. [12]. It was found that the densification behavior and the attendant microstructure of the as-processed parts were highly dependent on the laser power and laser scanning speed. Xiao investigated the effect of the rescanning cycles on the relative density, the microstructure, the residual stress and the mechanical properties of the SLM-processed Ti6Al4V material [13]. The relative density of the solidified parts was changed with the rescanning number and, the elongations of the as-fabricated parts were highly dependent on the porosity. To produce components with the high density, the Taguchi method through a statistical design was proposed by Sun et al. to optimize the processing parameters and modify the densification behavior based on the linear relationship among the relative density and the processing parameters [14]. The influence of the processing parameters on the surface quality of the SLM-processed 316L parts has been studied by Dursun et al. [15] and, it was found that the surface morphology and metallurgical defects were fundamentally determined by the laser power and the scan speed. Therefore, it could be concluded that the processing parameters played an important role in the formation of the densification behavior, the surface morphology and the final performance of the as-fabricated parts. However, through the experimental methods, it seemed that there existed a large challenge in discovering the powder metal melting behavior, the spreading procedure, the surface morphology evolution and the densification behavior within the molten pool irradiated by the high energy laser beam. Numerical simulation is an efficient method to investigate the heat and mass transfer and the melt convection during SLM and, it is vital to understand the mechanisms of the surface morphology evolution and the formation of the metallurgical defects. The 2D/3D numerically programmed models were established by Körner et al. using the Lattice Boltzmann Method (LBM) to study the melting and solidification process of powder material [16,17] and, the capillary and wetting phenomena of the molten pool were studied. The physical phenomena including the powder melting behavior, the thermocapillary convection and the material evaporation during the SLM of 316L stainless steel were studied by King et al. using their home-made code [18] and, the mechanisms of the pore defects, the material spattering and the denudation

zones were revealed. However, it seemed that the relationships of the processing parameters and the physical phenomena were not provided. Meanwhile, Wei et al. have pointed out that the recoil pressure played an important role in the heat and mass transfer within the molten pool [19]. Therefore, the recoil pressure should be considered in the physical model and, the melt convection and the formation of the potential defects affecting the forming quality were worth to be discovered.

In this study, the three-dimensional physical model of the randomly packed powder material fabricated by SLM process was established, taking into account the transformation of the material phase, the melt spreading and the interaction of the free surface of the molten pool and the recoil pressure caused by the material evaporation. The effect of the processing parameters on the melting behavior of the powder material, the melt convection, the surface morphology evolution and the densification behavior during the SLM process was studied. The relationship of the densification and the surface morphology driven by the Marangoni convection and the recoil pressure was revealed.

2 Modeling and Experimental Procedures

2.1 Physical Model

During the SLM process, the loose powder material is irradiated by the high energy laser beam, indicating that there exists a complex interaction between the laser beam and the powder materials. A schematic of SLM physical model is depicted in Fig. 1, including the melting and solidification, the phase transformation, the multi-modes of the heat transmission (the conduction, the radiation, the convection) and the variation of the thermophysical properties of metal materials, including the viscosity, the surface tension and the thermal conductivity.

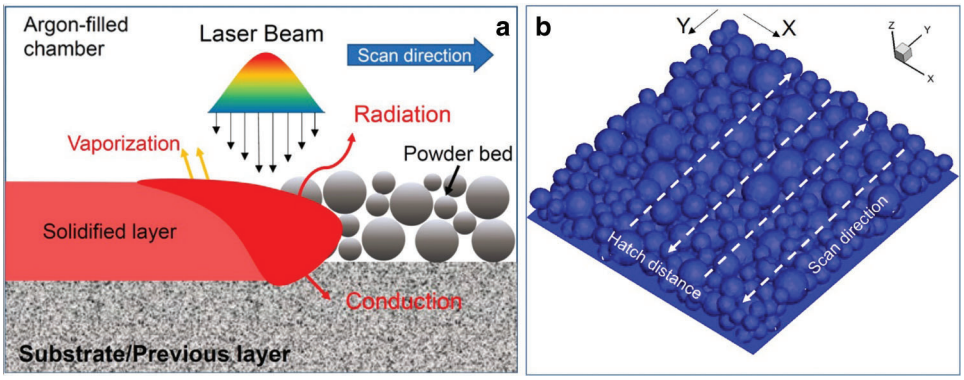

Figure 1: Schematic of SLM physical model (a); establishment of randomly packed powder-bed model (b)

Based on the established physical phenomena, a mesoscale computational fluid dynamics (CFD) model was developed with a three dimension of 300 × 300 × 90 μm^3, as shown in Fig. 1b. The geometric powder bed model was composed of the powder particles and the previous layer/substrate of the Ti material. For the accurate reproduction of the powder deposited bed, the metallic powders were randomly generated by the random algorithm in MATLAB to prevent the overlap, excessive gap and some anti-physical phenomena. The powder particles within a range of radius were produced in the certain powder thickness. To rationalize the fluid flow within the molten pool, an improved volume of fluid (VOF) method was applied to solve the coupling of Navier-Stokes equation, Energy conservation, Continuity equation and VOF equation, along with the evolution of the liquid/gas free interface. Based on the VOF calculation, two phases were considered: one phase was the randomly packed metallic powder and the metal substrate. The other was filled with the protection argon gas where the rest regions in the established physical model. The multi-track scanning strategy was also considered, as illustrated in Fig. 1b. Based on the

investigations [20], the dynamic viscosity, the thermal conductivity and the surface tension of the melt were regarded as the function of the operating temperature, including the step change of the solid-liquid transition. The other thermal physical properties of the applied material were assumed to be constant.

2.2 Governing Equations

In the CFD model, four basic physical governing equations, followed by the conservation of the mass, the momentum and the energy equation, were described as follows [21]. The laser heat source with a volumetric Gaussian distribution was from research [22]. The recoil pressure was produced by the vaporization of the molten material, and it could be derived from the Clausius-Clapeyron equation [23].

Based on the VOF model applied in this two-phase-system simulation, the volume-fraction-averaged material properties are calculated by:

$$\bar{x} = \alpha_1 x_1 + \alpha_2 x_2 \tag{1}$$

$$\alpha_1 + \alpha_2 = 1 \tag{2}$$

And the volume fraction equation for i phase is

$$\frac{\partial \alpha_i}{\partial t} + \vec{v} \cdot \nabla \alpha_i = \frac{S_{\alpha_i}}{\rho_i} \tag{3}$$

where α_i represents the volume fraction of i phase.

2.3 Boundary Conditions

Considering the radiation and the convection, the boundary condition at the wall was given by Dai et al. [24]. The side wall and the bottom wall were settled as the thermal convection wall with the heat transfer coefficient equal to 10 W/m^{2}K. The thermophysical properties of the applied material are shown in Fig. 2 [25], and the thermal conductivity of the powder material was calculated based on the work [26].

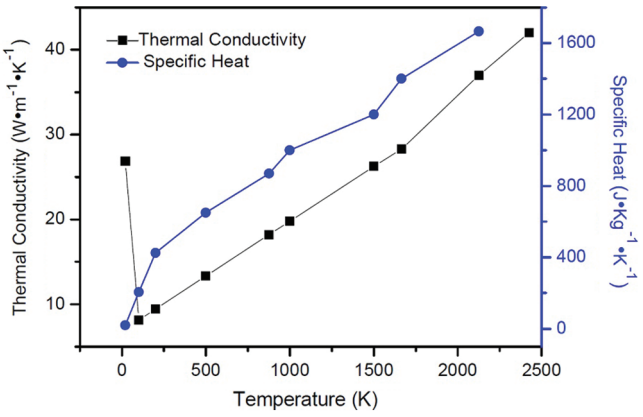

Figure 2: Thermophysical properties of Ti6Al4V material applied in the calculation

2.4 Experimental Procedures

In this study, the Ti6Al4V powder with a nearly spherical shape and an average diameter of 25 μm was used as the raw material. The SLM process system was self-developed and mainly consisted of a YLR-500 ytterbium fiber laser with a maximum laser power of 500 W and a laser spot size of 70 μm (IPG Laser GmbH, Burbach, Germany), an automatic powder layering device, an inert argon gas protection system, and a

Table 1: As-used experimental SLM processing parameters

Parameter	Value
Powder layer thickness	30 μm
Laser power	250 W
Radius of laser beam	35 μm
Scan speed	1000, 800, 600, 400 mm/s
Diameter range of powder	Ti6Al4V 15~43 μm

computer system for processing controlling. To further validate the accuracy and validity of the physical model, the experimental processing parameters were in a full accordance with those applied for numerical simulation (Tab. 1). The pressure of the argon gas within the processing chamber was settled as a constant of 0.7 kPa throughout the experiments. The surface morphologies of single tracks fabricated by the SLM process were observed by scanning electron microscope (COXEM-30 Plus).

3 Results and Discussion

3.1 Operating Temperature and Surface Morphology Evolution

Fig. 3 depicts the temperature contour and the surface morphology of the molten pool along the laser scan direction using different processing parameters. The maximum temperature and the width of the molten pool were increased with the application of the high energy density. For the laser energy density of 167 J/mm^3, the maximum operating temperature of 2100 K within the molten pool was obtained, which was slightly higher than the liquidus temperature of Ti6Al4V (1928 K), resulting in the partial melting of the powder material and the resultant discontinuous track combined with the rough surface (Fig. 3a). The residual pores had a high tendency to be produced on the top surface. As the laser energy density increased to 208 J/mm^3, the surface of the scan track, appeared with some residual pores, became smooth with the maximum temperature as high as 3100 K, implying the occurrence of the enhanced melting behavior of the powder material (Fig. 3b). For the laser energy density of 277 J/mm^3, the surface

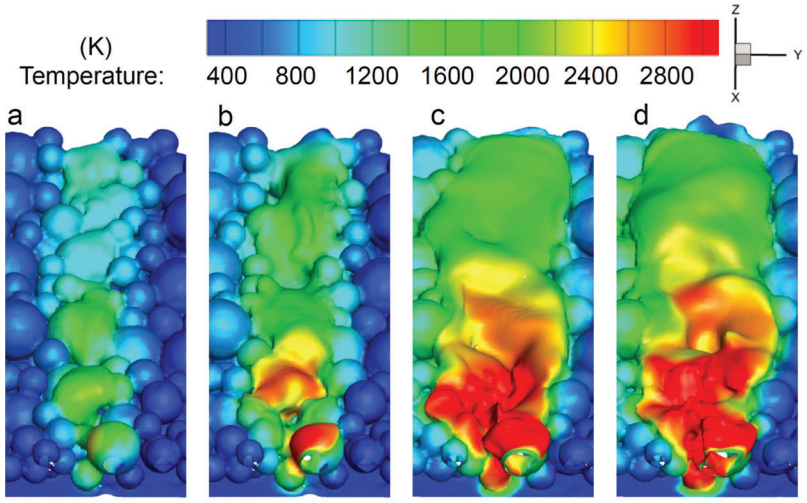

Figure 3: Operating temperature of the top surface within the molten pool obtained in the laser scanned tracks using different processing parameters: (a) v = 1000 mm/s, η = 167 J/mm^3; (b) v = 800 mm/s, η = 208 J/mm^3; (c) v = 600 mm/s, η = 277 J/mm^3 and (d) v = 400 mm/s, η = 417 J/mm^3

morphology of the solidified part was shown in the dense and smooth pattern combined with the maximum temperature of the molten pool reaching 3100 K, leading to the formation of the complete melting of the powder material and the uniform width of the scan track (Fig. 3c). As the applied laser energy density was further increased to 417 J/mm^3, the melting behavior of the powder material was maintained with the maximum operating temperature of 3100 K, while it seemed that the disturbance of the molten pool was considerably increased with the formation of the residual pores located in the rear region of the molten pool (Fig. 3d). In this situation, the melt tended to splash due to the unstability of the molten pool, which was detrimental to the surface morphology. It might be mainly derived from the enhanced thermocapillary convection within the molten pool caused by the sufficient irradiation of the laser energy, the higher surface tension gradient and the reduced viscosity.

In order to have a thorough understanding of the operating temperature distribution on the free surface of the molten pool, the temperature curves of the molten pool along the laser scan direction are depicted in Fig. 4. The operating temperature on the free surface of the molten pool had an apparent temperature gradient from the irradiation center to the edge of the molten pool. For the laser energy density of 167 J/mm^3, the minimum temperature of the plateau in the rear region and the peak temperature were 1100 K and 2100 K, respectively. Meanwhile, some valley temperatures with the mean value of 500 K, considerably below the liquidus temperature of Ti6Al4V material, were obtained, implying the generation of the non-melting of the powder material and the insufficient melt wetting behavior due to the limited volume of molten pool (Fig. 3a). As the laser energy density was increased to 208 J/mm^3, the peak temperature was increased to 3000 K combined with the plateau temperature of 1500 K. The valley temperature near the molten pool was increased to 1600 K, indicating that the enhanced melting behavior of the powder material and the melt wetting behavior happened. For the laser energy density of 277 J/mm^3, the valley and the plateau of the temperature curves were obviously disappeared with the formation of the peak temperature of 3400 K, which was mainly derived from the sufficient laser irradiation, the generation of full volume of molten pool and the efficient melt spreading (Fig. 3c). As the applied laser energy density was further increased to 417 J/mm^3, the maximum temperature of the molten pool was as high as 4000 K, which was far more than the vaporization point of Ti6Al4V material (3315 K). Meanwhile, the valley temperature within the molten pool was discovered, implying the unstable state of the molten pool. Therefore, the serious melt fluctuation was generated due to the decreased viscosity and the higher temperature gradient, resulting in the formation of the uneven surface morphology (Fig. 3d).

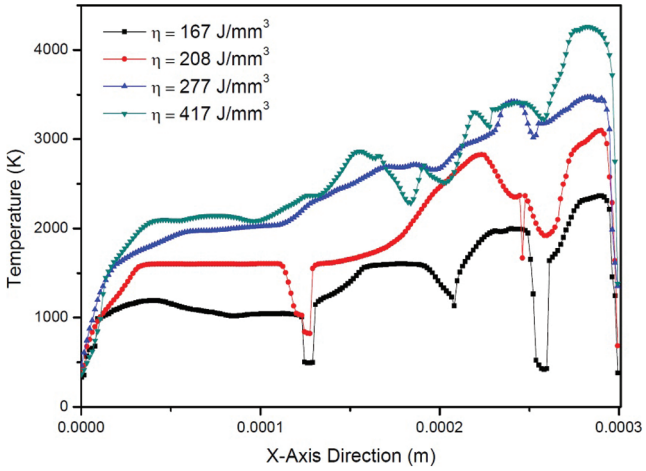

Figure 4: Operating temperature curves predicted on the top surface of the molten pool using different processing parameters

3.2 Laser Energy Effect Depth and Material Melting Behavior

The laser energy effect depth along the molten pool depth played a key role in the material melting behavior, determining the metallurgical bonding ability of the scan track and the substrate. Fig. 5 shows the temperature contour along the longitudinal direction using different processing parameters. For the laser energy density of 167 J/mm^3, the laser energy effect depth was nearly equal to the powder layer thickness and, the operating temperature of the substrate was only 800 K (Fig. 5a). As a result, the residual pores and the poor bonding behavior had a high tendency to be generated.

As the laser energy density was increased to 208 J/mm^3, the separated regions of the temperature within the molten pool above the liquidous temperature of Ti6Al4V material were enlarged. Meanwhile, the laser energy effect depth was slightly increased with the operating temperature of the substrate reaching 1200 K (Fig. 5b). However, the metallurgical defects, the residual pores and the partial melting of the powder material, would happen due to the limited depth of the molten pool and the restricted spreading behavior. For the laser energy density of 277 J/mm^3, the continuous and enlarged region in the laser irradiation was obtained with the maximum temperature of 3200 K (Fig. 5c). Meanwhile, it was interesting to find that the temperature of the substrate was increased with the value of 2000 K, implying that the laser energy effect depth was larger than the thickness of the powder layer. Therefore, the formation of the metallurgical bonding ability between the substrate and the deposited layer was reasonably obtained due to the efficient laser energy effect depth. As the applied laser energy density was further increased to 417 J/mm^3, the temperature located in the connection area of the deposited track and the substrate was equal

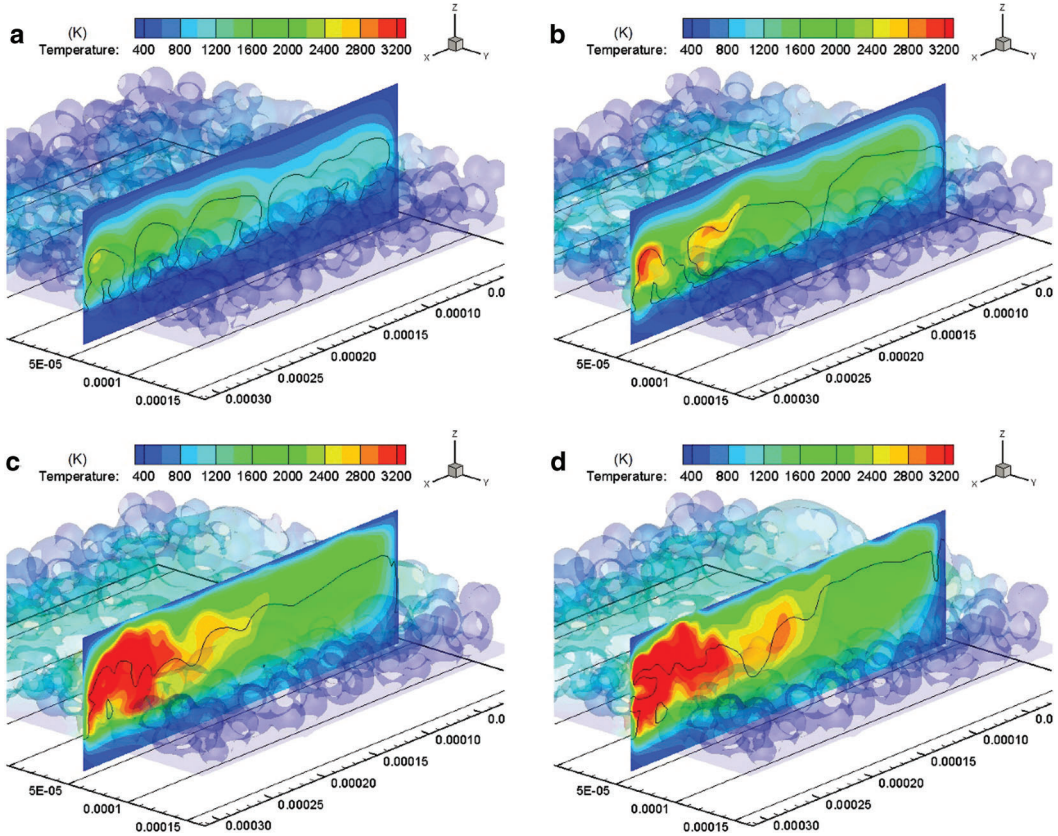

Figure 5: Operating temperature of the molten pool and the protection gas along the longitudinal direction using different processing parameters: (a) v = 1000 mm/s, η = 167 J/mm^3; (b) v = 800 mm/s, η = 208 J/mm^3; (c) v = 600 mm/s, η = 277 J/mm^3 and (d) v = 400 mm/s, η = 417 J/mm^3

to 1300 K, assuring the formation of the fine bonding behavior in the successive layers. Meanwhile, the maximum temperature was not only appeared within the molten pool, but also found in the protection gas region, implying the occurrence of the material vaporization (Fig. 5d). As a result, the serious fluctuation of the molten pool was obtained with the appearance of the recoiling pressure caused by the material evaporation, enhancing the potential of the collapse of the molten pool and the generation of the residual pores.

The detailed information of the temperature distribution and the temperature gradient along the molten pool depth using different processing parameters is shown in Fig. 6. The maximum temperature along the molten pool depth had a positive relationship with the laser energy density and, the maximum temperature was obtained near the free surface of the molten pool combined with the decrease trend along the molten pool depth. For the laser energy density of 167 J/mm^3, the temperature decreased linearly with the increase in the distance from the free surface to the bottom of the molten pool where the temperature was equal to the ambient temperature of 300 K and, the laser energy effect depth was 35 μm, which was nearly equal to the layer thickness (Fig. 6a). As the laser energy density was increased to 208 J/mm^3, the linear relationship of the operating temperature and the depth of the molten pool was maintained and, the occurrence of the heat accumulation within the molten pool was obtained. Therefore, the heat dissipation rate through the thermal conduction, the heat convection and the heat irradiation was transformed, leading to the formation of the large region of the molten pool and the increased energy effect depth (Fig. 6b). For the applied laser energy density of 277 J/mm^3, the temperature transformation trend along the molten pool depth was maintained with the laser energy effect depth of 45 μm, realizing the melting of the substrate (Fig. 6a). Meanwhile, the melt temperature within the laser irradiation region was as high as 3250 K, which was equal to the vaporization point of Ti6Al4V material (3315 K). As the applied laser energy density was increased to 417 J/mm^3, the decrease trend of the temperature was maintained in the same pattern, while the valley temperature located in the free surface of the molten pool was obtained. Meanwhile, the maximum temperature was generated above the surface of the molten pool with the value of 4000 K, implying that the severe material vaporization was considerably produced. As a result, the phenomenon of the material vaporization was detrimental to the surface morphology and the resultant densification behavior [20,23]. The temperature gradient near the free surface of the molten pool was fluctuated between 0 and 2.5 × 10^7 K/m for the laser energy density ranging from 167 J/mm^3 to 208 J/mm^3. As the laser energy density was increased to 277 J/mm^3, the temperature gradient near the free surface of the molten pool was increased towards to the bottom of the molten pool, reaching the maximum value of 1.0 × 10^8 K/m and promoting to the generation of the desired surface tension. As the

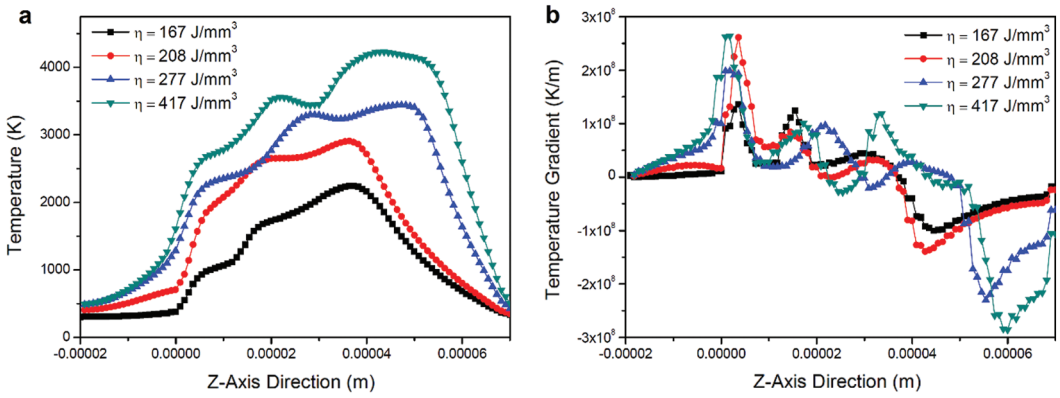

Figure 6: Temperature curves (a) and the temperature gradient (b) predicted along the laser penetration depth direction using different processing parameters

applied laser energy density increased to 417 J/mm^3, the temperature gradient in the neighboring area of the molten pool originally underwent the opposite trend with the formation of the negative temperature gradient and then, the trend turned to the positive value and reached the maximum value of 1.2×10^8 K/m (Fig. 6b), caused by the formation of the material vaporization (Fig. 5d). For the connection region near the substrate, the maximum temperature gradient was obtained due to the efficient heat diffusion.

3.3 Densification Behavior and Melt Wetting Ability with the Substrate

The densification behavior in the connection region and the stable fabrication of the whole parts was sensitive to the melt wetting ability with the substrate or the as-processed layer. The densification behavior and the residual pores within the longitudinal-sections using different processing parameters are shown in Fig. 7. For the applied laser energy density of 167 J/mm^3, the powder particles were partially melted and the attendant residual pores with the irregular patterns were located in the connection region of the deposited track and the substrate (Fig. 7a), resulting in the formation of the continuous gaps within the solidified parts. Therefore, the metallurgical bonding ability of the deposited layers was poor, having a negative effect on the powder bed quality caused by the interaction of the spalling layer with the scraper. As the laser energy density was increased to 208 J/mm^3, the metallurgical bonding ability with the deposited layer and the as-processed part was apparently enhanced with the decreased number and size of the residual pores (Fig. 7b), implying the increased volume of the melt caused by the increased laser energy effect depth (Fig. 5b). For the laser energy density of 277 J/mm^3, the densification behavior

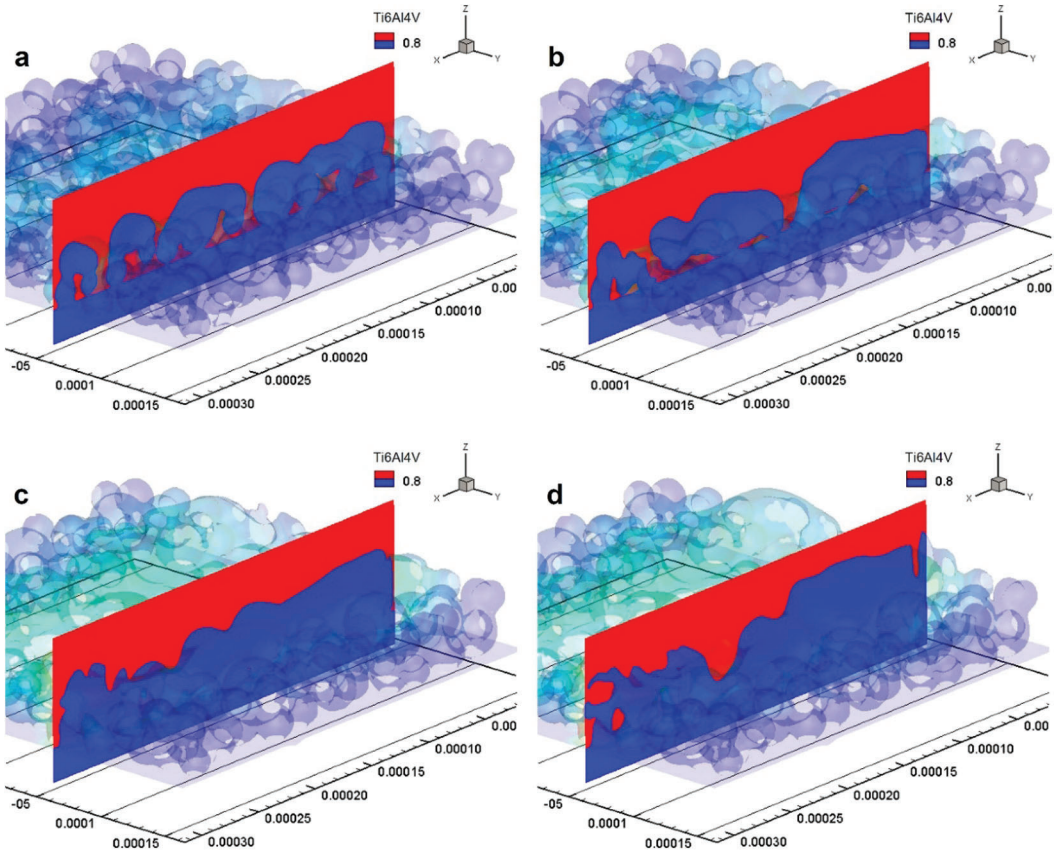

Figure 7: Densification behavior and residual pores along the longitudinal direction using different processing parameters (P = 250 W): (a) v = 1000 mm/s, η = 167 J/mm^3; (b) v = 800 mm/s, η = 208 J/mm^3; (c) v = 600 mm/s, η = 277 J/mm^3 and (d) v = 400 mm/s, η = 417 J/mm^3

of the longitudinal-sections of the solidified part was considerably increased with the disappearance of the residual pores (Fig. 7c) and, the excellent bonding ability, derived from the efficient melting of the powder material and the wetting behavior with the substrate, was obtained. Meanwhile, the surface morphology of the solidified part was fluctuated with the elimination of the penetrated pores. As the applied laser energy density was further increased to 417 J/mm^3, the wetting behavior and the densification of the solidified part were fine while, the serious fluctuation of the free surface of the molten pool was generated due to the material evaporation and the attendant recoil pressure (Fig. 6a). The unstable molten pool had a high tendency to produce the irregular pores caused by the collapse of the molten pool and the entrapment of the gas phase (Fig. 7d). As a result, a large roughness of the top surface and a decreased relative density was obtained.

The surface morphology evolution and the densification behavior of the solidified part were sensitive to the velocity vector of the free surface within the molten pool. The velocity vectors of the free surface of the molten pool using different processing parameters are shown in Fig. 8. The velocity distribution of the free surface of the molten pool along the laser scan direction is shown in Fig. 9. For the application of the laser energy density of 167 J/mm^3, the velocity vector of the free surface was pretty blurry and the velocity value was considerably tiny (Fig. 8a), which was caused by the higher melt viscosity and the restricted surface tension gradient. The mean velocity was about 0.6 m/s. As the laser energy density was increased to 208 J/mm^3, the velocity vector of the melt was shown in the radially outward pattern (Fig. 8b). The mean

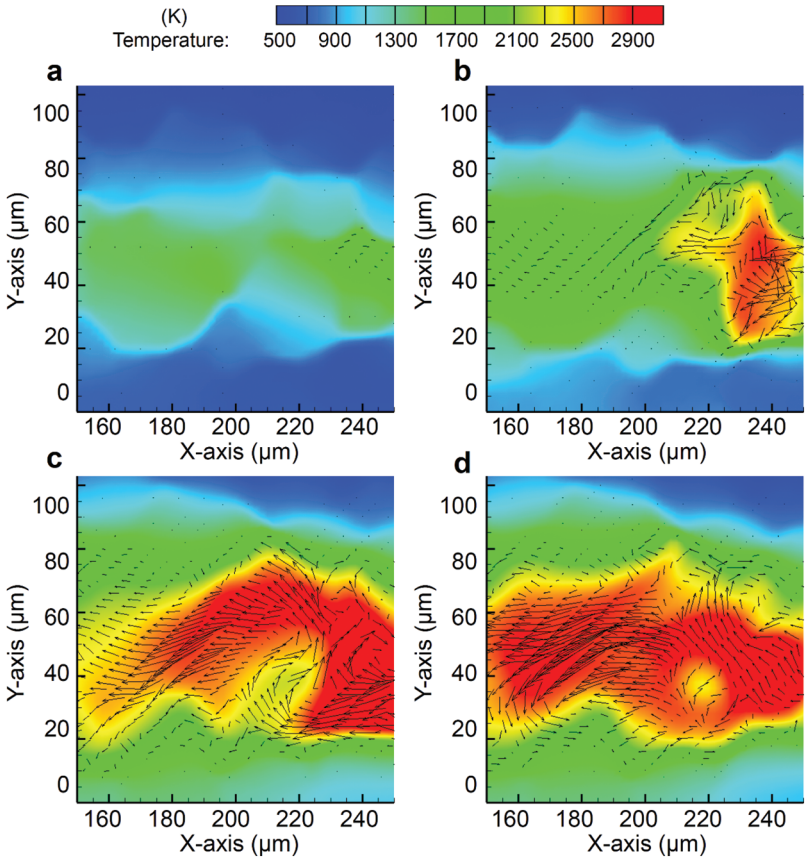

Figure 8: Velocity vector obtained within the molten pool using different processing parameters: (a) v = 1000 mm/s, η = 167 J/mm^3; (b) v = 800 mm/s, η = 208 J/mm^3; (c) v = 600 mm/s, η = 277 J/mm^3 and (d) v = 400 mm/s, η = 417 J/mm^3

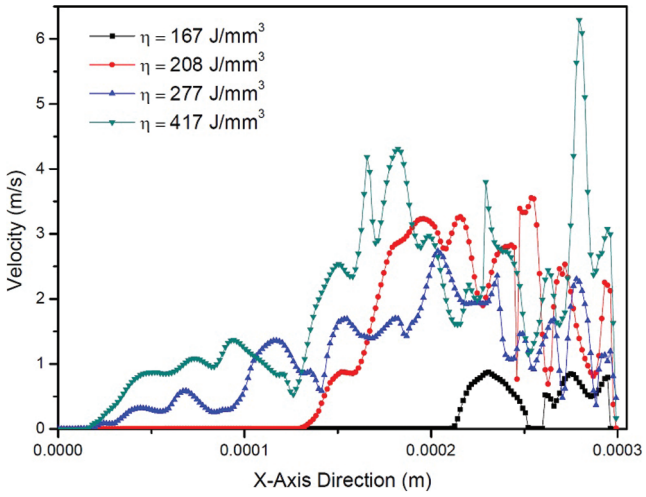

Figure 9: Velocity distribution on the free surface of the molten pool along the laser scan direction using different processing parameters

melt velocity was 1.5 m/s combined with the apparent value fluctuation (Fig. 9), indicating the efficient transportation and wetting of the melt. For the applied laser energy density of 277 J/mm^3, the velocity vector towards to the rear region of the molten pool was generated and meanwhile, the vortex vector of the melt in the irradiated region promoted the melt convection to the edge region of the molten pool, enhancing the energy dissipation from the center of the molten pool and the resultant production of the sufficient volume of melt (Fig. 8c). As the applied laser energy density was further increased to 417 J/mm^3, the velocity vector in the irradiated region was shown in the radially outward direction with the maximum velocity value of 6 m/s (Figs. 8d and 9), implying the formation of the serious material evaporation and the fluctuation of the molten pool. Therefore, the surface quality and the spreading behavior of the molten pool were negatively controlled. Therefore, it could be concluded that the intensive velocity vector showed an improved wetting and spreading behavior, which contributed to the variation of the surface morphology and the motion of the gas phase within the molten pool for the densification behavior.

3.4 Experimental Verification

The surface morphology of the laser scan track using different processing parameters is shown in Fig. 10. For the application of the laser energy density of 167 J/mm^3, the solidified track was shown in the broken drops (Fig. 10a), which was consistent with the discontinuous tracks predicted by the simulation (Fig. 3a). The contraction was appeared in the both ends of the solidified broken tracks, which was caused the compromising interaction between the surface tension and the melt viscosity (Fig. 8a). As the laser energy density was increased to 208 J/mm^3, the continuous track was obtained with the appearance of the apparent necks due to the melt shrinkage behavior (Fig. 10b). In this situation, it could be confirmed that the melt disturbance was enhanced caused by the enhanced temperature gradient (Fig. 6b). For the laser energy density of 277 J/mm^3, the uniform width of the continuous scan track was obtained (Fig. 10c), which was caused by the generation of the velocity vector towards to the rear region of the molten pool and the attendant wetting behavior of the melt (Fig. 8c). As the laser energy was further increased to 417 J/mm^3, the continuous track was obtained while, some tiny drops were appeared on the solidified surface of the scan track combined with the disappearance of the uniform width of the scan track (Fig. 10d), which was mainly caused by the formation of the enhanced melt disturbance due to the material evaporation and the attendant recoiling pressure (Figs. 8d and 9).

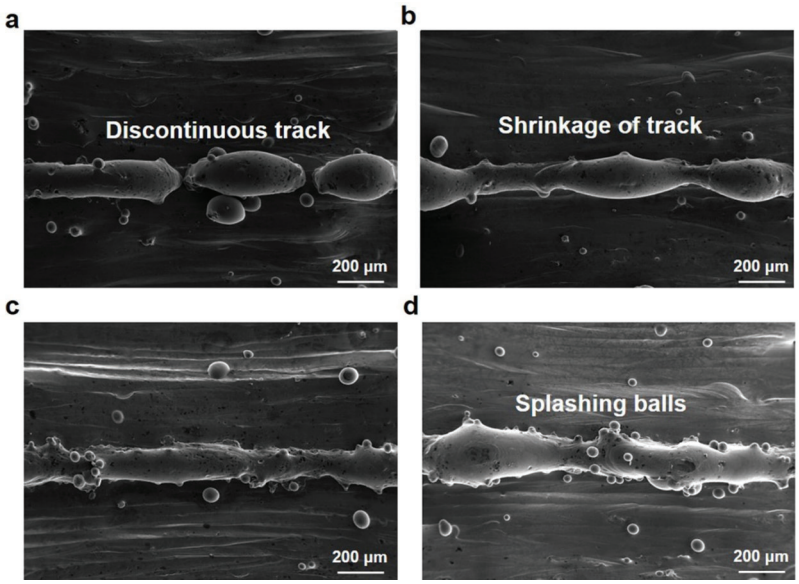

Figure 10: Surface morphology of the laser scan track using different processing parameters: (a) v = 1000 mm/s, η = 167 J/mm^3; (b) v = 800 mm/s, η = 208 J/mm^3; (c) v = 600 mm/s, η = 277 J/mm^3 and (d) v = 400 mm/s, η = 417 J/mm^3

4 Conclusions

The simulation of the thermodynamics behavior within the molten pool and the surface morphology evolution during selective laser melting of Titanium alloy Ti6Al4V has been performed. The laser energy effect depth, the melt convection, the metallurgical bonding ability and the mechanisms of the surface morphology evolution and the densification behavior were revealed.

1. The surface underwent the typical change from the discontinuous track with the rough surface to the continuous tracks with residual porosities, then to the continuous tracks with the dense surface and finally to the fluctuated tracks with collapsed pores were generated with the increase in the applied laser energy density.
2. The maximum temperature and the plateau temperature were obtained as the laser energy density was low and, some valley temperatures were generated, implying the different melting behavior of the powder material. While as the laser energy density was too high, the severe material evaporation would happen combined with the appearance of the plateau temperature, disturbing the melt convection. In the optimized laser energy density, the efficient melt convection and the spreading would promote the formation of the fine surface morphology and the relative density.
3. The laser energy effect depth played an important role in the formation of the metallurgical bonding ability between the molten pool and the substrate or the as-processed layer. The irregular pores or the collapsed pores in the connection region caused by the partial melting of the powder material or the collapse of the molten pool due to the recoil pressure were obtained.

Funding Statement: We are grateful for the financial support from the National Key Research and Development Program “Additive Manufacturing and Laser Manufacturing” (Nos. 2016YFB1100101, 2018YFB1106302); the National Natural Science Foundation of China (Nos. 51790175, 51735005); the Fundamental Research Funds for the Central Universities (No. NC2020004), the financial support from the Innovation Fund of National Engineering and Research Center for Commercial Aircraft Manufacturing (No. COMAC-SFGS-2016-33238); National Natural Science Foundation of China for

Creative Research Groups (Grant No. 51921003); The 15th Batch of "Six Talents Peaks" Innovative Talents Team Program "Laser Precise Additive Manufacturing of Structure-Performance Integrated Lightweight Alloy Components" (No. TD-GDZB-001) (Jiangsu Provincial Department of Human Resources and Social Security of China); 2017 Excellent Scientific and Technological Innovation Teams of Universities in Jiangsu "Laser Additive Manufacturing Technologies for Metallic Components" (Jiangsu Provincial Department of Education of China).

Conflicts of Interest: The authors declare that they have no conflicts of interest to report regarding the present study.

References

1. Yadroitsev, I., Krakhmalev, P., Yadroitsava, I. (2014). Selective laser melting of Ti6Al4V alloy for biomedical applications: temperature monitoring and microstructural evolution. *Journal of Alloys and Compounds, 583,* 404–409. DOI 10.1016/j.jallcom.2013.08.183.
2. Sun, J., Yang, Y., Wang, D. (2013). Mechanical properties of a Ti6Al4V porous structure produced by selective laser melting. *Materials & Design, 49,* 545–552. DOI 10.1016/j.matdes.2013.01.038.
3. Chen, C., Hao, Y., Bai, X., Ni, J., Chung, S. et al. (2019). 3D printed porous Ti6Al4V cage: effects of additive angle on surface properties and biocompatibility; bone ingrowth in Beagle tibia model. *Materials & Design, 175,* 107824. DOI 10.1016/j.matdes.2019.107824.
4. Shipley, H., McDonnell, D., Culleton, M., Coull, R., Lupoi, R. et al. (2018). Optimisation of process parameters to address fundamental challenges during selective laser melting of Ti-6Al-4V: a review. *International Journal of Machine Tools and Manufacture, 128,* 1–20. DOI 10.1016/j.ijmachtools.2018.01.003.
5. Gu, D., Meiners, W., Wissenbach, K., Poprawe, R. (2013). Laser additive manufacturing of metallic components: materials, processes and mechanisms. *International Materials Reviews, 57(3),* 133–164. DOI 10.1179/1743280411Y.0000000014.
6. Zhang, J., Song, B., Wei, Q., Bourell, D., Shi, Y. (2019). A review of selective laser melting of aluminum alloys: processing, microstructure, property and developing trends. *Journal of Materials Science and Technology, 35(2),* 270–284. DOI 10.1016/j.jmst.2018.09.004.
7. Wang, D., Song, C., Yang, Y., Bai, Y. (2016). Investigation of crystal growth mechanism during selective laser melting and mechanical property characterization of 316L stainless steel parts. *Materials & Design, 100,* 291–299. DOI 10.1016/j.matdes.2016.03.111.
8. Li, R., Wang, M., Yuan, T., Song, B., Chen, C. et al. (2017). Selective laser melting of a novel Sc and Zr modified Al-6.2Mg alloy: processing, microstructure, and properties. *Powder Technology, 319,* 117–128. DOI 10.1016/j.powtec.2017.06.050.
9. Gu, D., Xia, M., Dai, D. (2019). On the role of powder flow behavior in fluid thermodynamics and laser processability of Ni-based composites by selective laser melting. *International Journal of Machine Tools and Manufacture, 137,* 67–78. DOI 10.1016/j.ijmachtools.2018.10.006.
10. Dai, D., Gu, D. (2015). Tailoring surface quality through mass and momentum transfer modeling using a volume of fluid method in selective laser melting of TiC/AlSi10Mg powder. *International Journal of Machine Tools and Manufacture, 88,* 95–107. DOI 10.1016/j.ijmachtools.2014.09.010.
11. Yu, W., Sing, S., Chua, C., Kuo, C., Tian, X. (2019). Particle-reinforced metal matrix nanocomposites fabricated by selective laser melting: a state of the art review. *Progress in Materials Science, 104,* 330–379. DOI 10.1016/j.pmatsci.2019.04.006.
12. Song, B., Dong, S., Zhang, B., Liao, H., Coddet, C. (2012). Effects of processing parameters on microstructure and mechanical property of selective laser melted Ti6Al4V. *Materials & Design, 35,* 120–125. DOI 10.1016/j.matdes.2011.09.051.
13. Li, L. B., Li, R. D., Yuan, T. C., Chen, C., Li, X. F. (2020). Microstructures and tensile properties of a selective laser melted Al-Zn-Mg-Cu alloy by Si and Zr microalloying. *Materials Science and Engineering: A, 787,* 139492. DOI 10.1016/j.msea.2020.139492.

14. Sun, J., Yang, Y., Wang, D. (2013). Parametric optimization of selective laser melting for forming Ti6Al4V samples by Taguchi method. *Optics & Laser Technology, 49,* 118–124. DOI 10.1016/j.optlastec.2012.12.002.
15. Dursun, G., Ibekwe, S., Li, G., Mensah, P., Joshi, G. et al. (2020). Influence of laser processing parameters on the surface characteristics of 316L stainless steel manufactured by selective laser melting. *Materials Today: Proceedings, 26,* 387–393. DOI 10.1016/j.matpr.2019.12.061.
16. Körner, C., Attar, E., Heinl, P. (2011). Mesoscopic simulation of selective beam melting processes. *Journal of Materials Processing Technology, 211(6),* 978–987. DOI 10.1016/j.jmatprotec.2010.12.016.
17. Ammer, R., Markl, M., Ljungblad, U., Körner, C., Rüde, U. (2014). Simulating fast electron beam melting with a parallel thermal free surface lattice Boltzmann method. *Computers and Mathematics with Applications, 67(2),* 318–330. DOI 10.1016/j.camwa.2013.10.001.
18. Khairallah, S. A., Anderson, A. T., Rubenchik, A., King, W. E. (2016). Laser powder-bed fusion additive manufacturing: physics of complex melt flow and formation mechanisms of pores, spatter, and denudation zones. *Acta Materialia, 108,* 36–45. DOI 10.1016/j.actamat.2016.02.014.
19. Zheng, M., Wei, L., Chen, J., Zhang, Q., Zhong, C. et al. (2019). A novel method for the molten pool and porosity formation modelling in selective laser melting. *International Journal of Heat and Mass Transfer, 140,* 1091–1105. DOI 10.1016/j.ijheatmasstransfer.2019.06.038.
20. Yuan, W. H., Chen, H., Cheng, T., Wei, Q. S. (2020). Effects of laser scanning speeds on different states of the molten pool during selective laser melting: simulation and experiment. *Materials & Design, 189,* 108542. DOI 10.1016/j.matdes.2020.108542.
21. Wang, L., Jia, S., Liu, Y., Chen, B., Yang, D. et al. (2010). Modeling and simulation of anode melting pool flow under the action of high-current vacuum arc. *Journal of Applied Physics, 107(11),* 113306. DOI 10.1063/1.3386568.
22. Xia, M., Gu, D., Yu, G., Dai, D., Chen, H. et al. (2017). Porosity evolution and its thermodynamic mechanism of randomly packed powder-bed during selective laser melting of Inconel 718 alloy. *International Journal of Machine Tools and Manufacture, 116,* 96–106. DOI 10.1016/j.ijmachtools.2017.01.005.
23. Cho, J. H., Na, S. J. (2006). Implementation of real-time multiple reflection and Fresnel absorption of laser beam in keyhole. *Journal of Physics D: Applied Physics, 39(24),* 5372–5378. DOI 10.1088/0022-3727/39/24/039.
24. Dai, D., Gu, D. (2014). Thermal behavior and densification mechanism during selective laser melting of copper matrix composites: simulation and experiments. *Materials & Design, 55,* 482–491. DOI 10.1016/j.matdes.2013.10.006.
25. Yan, W., Ge, W., Qian, Y., Lin, S., Zhou, B. et al. (2017). Multi-physics modeling of single/multiple-track defect mechanisms in electron beam selective melting. *Acta Materialia, 134,* 324–333. DOI 10.1016/j.actamat.2017.05.061.
26. Yang, J., Wang, F. (2009). 3D finite element temperature field modelling for direct laser fabrication. *International Journal of Advanced Manufacturing Technology, 43(11–12),* 1060–1068. DOI 10.1007/s00170-008-1785-x.